Simultaneous MR/PET Imaging of the Human Brain: Feasibility Study[1]

Heinz-Peter W. Schlemmer, MD, PhD
Bernd J. Pichler, MD
Matthias Schmand, PhD
Ziad Burbar, MD
Christian Michel, MD
Ralf Ladebeck, MD
Kirstin Jattke, MD
David Townsend, PhD
Claude Nahmias, MD
Pradeep K. Jacob, MD
Wolf-Dieter Heiss, MD
Claus D. Claussen, MD

The purpose of this study was to apply a magnetic resonance (MR) imaging–compatible positron emission tomographic (PET) detector technology for simultaneous MR/PET imaging of the human brain and skull base. The PET detector ring consists of lutetium oxyorthosilicate (LSO) scintillation crystals in combination with avalanche photodiodes (APDs) mounted in a clinical 3-T MR imager with use of the birdcage transmit/receive head coil. Following phantom studies, two patients were simultaneously examined by using fluorine 18 fluorodeoxyglucose (FDG) PET and MR imaging and spectroscopy. MR/PET data enabled accurate coregistration of morphologic and multifunctional information. Simultaneous MR/PET imaging is feasible in humans, opening up new possibilities for the emerging field of molecular imaging.

[1] From the Department of Diagnostic Radiology, University Hospital Tübingen, Hoppe-Seyler-Strasse 3, D-72076 Tübingen, Germany (H.W.S., B.J.P., C.D.C.); Department of Molecular Imaging, Siemens Medical Solutions, Knoxville, Tenn (M.S., Z.B., C.M.); Department of Magnetic Resonance, Siemens Medical Solutions, Erlangen, Germany (R.L., K.J.); Molecular Imaging and Translational Research Program, University of Tennessee Graduate School of Medicine, Knoxville, Tenn (D.T., C.N.); Department of Radiology, University of Tennessee Medical Center, Knoxville, Tenn (P.K.J.); and Max Planck Institute for Neurological Research, Cologne, Germany (W.D.H.). Received November 12, 2007; revision requested January 23, 2008; revision received March 25; accepted April 21; final version accepted April 24. **Address correspondence to** H.P.S. (e-mail: *heinz-peter.schlemmer@med.uni-tuebingen.de*).

The comprehensive assessment of anatomic, functional and molecular information is essential for molecular imaging. However, exact spatial correlation of imaging data acquired sequentially with separate scanners is limited, essentially because patient repositioning causes differing section orientations, as well as variations in organ shape and position. Several approaches for sophisticated image fusion by using affine and deformable transformations have been developed but combining image information by using visual comparison of images positioned side by side is still a commonly used approach in clinical practice. The most accurate data alignment can nevertheless be achieved by using hybrid systems enabling temporal and spatial coregistration of morphologic and functional data in a single examination and without repositioning the patient. A milestone was achieved in 1998 when the first integrated positron emission tomography (PET)/computed tomography (CT) scanner was introduced, combining functional PET with anatomic CT imaging in a single examination (1). Subsequently, PET/CT has been proved a powerful diagnostic tool in oncology for imaging a number of different tumors (eg, lung and head-and-neck tumors [2]), although PET and CT are still performed sequentially.

Magnetic resonance (MR) imaging has the distinct advantage, as compared with CT, of providing higher soft-tissue contrast that yields superior diagnostic accuracy, particularly in the brain, abdominal organs, and bone marrow (3,4). Particularly for brain imaging, simultaneous MR and PET imaging would enable a precise combination of morphologic, functional, and metabolic information for studying such processes as perfusion-dependent kinetics of tracer distribution. However, from a technologic point of view, simultaneous imaging was not feasible until now because conventional PET detectors are highly sensitive, even to small magnetic fields (5). However, new PET detector technology that is unaffected by the high magnetic field strength of the MR imaging system has been developed with lutetium oxyorthosilicate (LSO) scintillation crystals and avalanche photodiodes (APDs) (6,7). Recently, it has been shown that quantitative simultaneous MR/PET imaging is feasible in small animal systems (8).

The goal of this study was to demonstrate the feasibility of simultaneous MR/PET imaging of the human brain by using this PET detector technology integrated in a clinical 3.0-T MR imaging system.

Advance in Knowledge

- This technology enables simultaneous and isocentric MR/PET imaging of the human brain with image quality comparable to standalone systems.

Materials and Methods

Patients

Institutional Review Board approval was obtained for MR/PET examinations of patients with a history of cancer who had undergone routine clinical fluorine 18 fluorodeoxyglucose (FDG) PET/CT imaging for follow-up. Informed consent was obtained from each patient before the MR/PET examination, which immediately followed the PET/CT examination. In this study, two patients were examined: one with a history of malignant skin cancer and mild cognitive impairment and one with a history of thyroid cancer. The MR/PET examinations were performed in November 2006 (Siemens Medical Solutions, Knoxville, Tenn). The hardware and software components of the system were provided by Siemens (BrainPET; Erlangen, Germany). Several authors (M.S., Z.B., C.M., R.L., and K.J.) are employees of Siemens Medical Solutions (Knoxville, Tenn) and one author (W.D.H.) is a consultant for Siemens Medical Solutions (Knoxville, Tenn). All authors had control of the image data and postprocessing procedures, as well as all information used for the publication.

Implications for Patient Care

- The precise anatomic matching achieved enables the investigation of metabolism and function in small brain areas such as the nuclei of basal brain and brainstem.
- Simultaneous PET and functional MR imaging activation studies combined with diffusion tensor tracking may provide a deeper understanding of brain function.
- The effect of transmitter/receptor activation on perfusion may be analyzed by examining dynamic and perfusion-dependent kinetics of tracer/drug distribution in various brain structures.

PET Detector

The PET detector technology has been developed by using LSO scintillation crystals (7) and APDs (6,7) that can be operated within a high-field-strength MR imaging system. Each block detector consists of a 12 × 12 LSO matrix with an individual crystal size of 2.5 × 2.5 × 20 mm. The block is displayed on a 3 × 3 APD array with individual diodes that have an active surface of 5 × 5 mm. Six LSO-APD block detectors form a cassette and are arranged on the z axis of the scanner, forming 72 crystal rings. The entire PET scanner consists of 32 radially arranged cassettes and has an axial field of view (FOV) of about 19.2 cm and an inner ring diameter of 35.5 cm. The system has a time resolution of 5.6 msec (full width at half maximum) and a mean energy resolution at 511 keV of 22% (full

Published online
10.1148/radiol.2483071927

Radiology 2008; 248:1028–1035

Abbreviations:
APD = avalanche photodiodes
FDG = fluorine 18 fluorodeoxyglucose
FOV = field of view
HRRT = high-resolution research tomography
LSO = lutetium oxyorthosilicate

Author contributions:
Guarantors of integrity of entire study, H.W.S., D.T., C.D.C.; study concepts/study design or data acquisition or data analysis/interpretation, all authors; manuscript drafting or manuscript revision for important intellectual content, all authors; approval of final version of submitted manuscript, all authors; literature research, H.W.S., B.J.P., M.S., C.N., W.D.H.; clinical studies, H.W.S., D.T., C.N., P.K.J., W.D.H.; experimental studies, B.J.P., M.S., Z.B., C.M., R.L., K.J.; and manuscript editing, H.W.S., B.J.P., M.S., C.M., R.L., K.J., D.T., C.N., W.D.H., C.D.C.

See Materials and Methods for pertinent disclosures.

width at half maximum). All PET detector components such as amplifiers, resistors, shielding material, and housing were selected to minimize interference with the MR imaging B field, gradients, and radiofrequency. Large, solid, conductive materials were avoided to reduce the induction of eddy currents.

MR Imager

The MR-compatible PET detector ring was constructed to fit inside a standard clinical 3-T MR imager (TRIO; Siemens Medical Solutions) to match the two FOVs. Furthermore, a standard birdcage transmit/receive head coil (Siemens Medical Solutions) mounted on the MR imager bed could be placed inside the PET detector ring, thereby matching the two FOVs and enabling temporal and spatial registration of PET and MR data (Fig 1).

Combined MR/PET Imaging and Phantom Studies

Initial evaluation of the PET detector performance and of potential mutual interference between the PET and MR systems was undertaken by using a 20-cm-diameter cylindrical phantom filled with 37 MBq of FDG.

A Hoffman brain phantom, filled with 37 MBq of FDG, or alternatively, a high-resolution Cologne phantom (9,10) was placed in the MR/PET system. PET data were acquired for 30 minutes while MR imaging was performed by using a T2-weighted turbo spin-echo sequence. Potential artifacts caused by mutual interference between the PET and MR imaging system were qualitatively tested on the PET detector, the MR imaging signal level, and on image quality.

MR Sequence Protocol

The MR examination was performed during PET data acquisition. Conventional MR imaging of the brain included an axial T2-weighted turbo spin-echo sequence (repetition time msec/echo time msec, 4000/105; FOV, 216 × 240 mm; matrix size, 288 × 320; voxel size, 0.8 × 0.8 × 5.0 mm; and acquisition time, 2 minutes 8 seconds), a fluid-attenuated inversion recovery sequence (10 000/106; inversion time msec, 2500; FOV, 180 × 240 mm; matrix size, 168 × 320; voxel size, 1.1 × 0.8 × 5.0 mm; and acquisition time, 4 minutes 22 seconds), and a three-dimensional T1-weighted fast low-angle shot sequence (23/7.4; flip angle, 25°; FOV, 176 × 256 mm; matrix size, 176 × 256; voxel size, 1.0 × 1.0 × 1.0 mm; and acquisition time, 6 minutes 11 seconds). For diffusion-weighted imaging, a single-shot echo-planar imaging sequence was applied (3000/791; FOV, 240 × 240 mm; matrix size, 128 × 128; voxel size, 1.9 × 1.9 × 5.0 mm; acquisition time, 1 minute 11 seconds). Water diffusion was measured with a three-image trace technique by using b values of 0, 500, and 1000 sec/mm^2. Time-of-flight MR angiography was conducted at the level of the circle of Willis by using a three-dimensional fast low-angle shot sequence (22/3.7; flip angle, 18°; FOV, 150 × 200 mm; matrix size, 202 × 384; voxel size, 0.7 × 0.5 × 06 mm; and acquisition time, 4 minutes 19 seconds). For proton MR spectroscopy, two-dimensional spin-echo chemical shift imaging sequences were applied with a matrix size of 10 × 10 (point-resolved spectroscopy sequence for localization, elliptic k-space sampling). For patient 1, an echo time of 135 msec was chosen and the sequence was performed twice, in an axial orientation at the level of the ventricles and in a coronal orientation at the level of the hippocampus (1700/135; voxel size, 1.0 × 1.0 × 1.5 mm; number of excitations, 3; and acquisition time, 6 minutes 46 seconds). In patient 2, the imaging was performed on an axial orientation at the level of the ventricles (1700/30; voxel size, 0.75 × 1.0 × 1.5 mm; number of signals acquired, three; and acquisition time, 4 minutes 51 seconds). MR data were qualitatively evaluated regarding line broadening of resonances in proton MR spectra, as well as overall quality and potential artifacts of MR images.

PET Imaging

For PET imaging, the patients fasted for at least 4 hours before the intravenous injection of 370 MBq of FDG. The distribution of the tracer was recorded for 20 or 40 minutes at a steady state, 120 minutes after injection for the PET/CT scan at the University of Tennessee Medical Center (Knoxville, Tenn). Repeated multiple samples of arterial blood could not be obtained in the setting of this conceptual study and therefore, quantification of metabolic rates for glucose was not attempted. Data were acquired in 96-bit list mode containing complete information for each coincident event and were stored

Figure 1

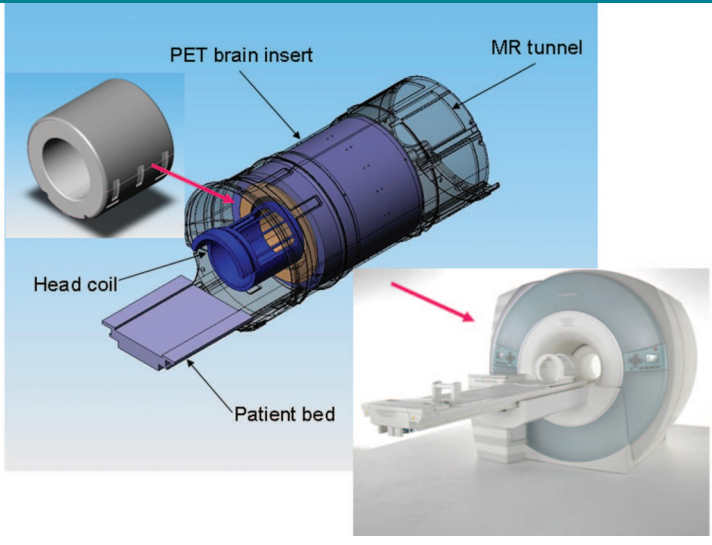

Figure 1: Drawing and photograph of integrated MR/PET design shows isocentric layering of MR head coil, PET detector ring, and tunnel of MR magnet.

on a disk, accumulating approximately 20 GB of raw data during the 40 minutes of acquisition. Prompt and random coincidences were then rebinned in sinograms in a high-resolution mode (span, 9; ring difference, 67), resulting in a three-dimensional data set of 1399 sinograms, each consisting of 256 angular projections and 192 radial elements. The data set was reconstructed iteratively (six iterations and 16 subsets) on a computer (approximately 12 seconds per iteration) by using an ordinary Poisson ordered subset expectation maximization three-dimensional (OPOSEM3D) algorithm (11) from prompt coincidences, normalization, attenuation, and expected random (12) and scatter (13) coincidences. The image volume consists of 153 transaxial image planes with a voxel size of 1.25 mm^3. Reconstructed resolution was 2.5 mm full width at half maximum in the center and 4.5 mm at 10 cm off axis (for a line source in air reconstructed by using OPOSEM3D). For attenuation correction, the image of the head obtained by using MR was segmented in air and tissue (bone was neglected). Labels were assigned to each region and were then converted to attenuation coefficients at 511 keV and forward projected. The normalization was calculated from four 8-hour plane source normal images. The plane source extending the cross section of the entire FOV was oriented in the z axis and rotated four times with a 36° step angle. The activity images of the volume of the brain were displayed in an orthogonal navigator (transaxial, sagittal, and frontal views) as multisection (volume) images. The VINCI (volume-imaging in neurological research, coregistration and ROIs included [14]) image fusion software allowed linear transformation and rotation to overlay the PET and MR images. This image fusion will be done in the future automatically by using a predetermined transformation matrix.

Results

PET Detector and MR Imager

The registration of annihilation photons by the scintillation crystals was not noticeably compromised either by the static magnetic field or by the simultaneous switching of radiofrequency and magnetic gradients. Flood images acquired with the PET detectors inside and outside MR imaging and while acquiring gradient-echo and spin-echo sequences showed no obvious degradation in the ability to identify the individual crystals and their energy spectra within the detector blocks. Energy resolution remained constant for the blocks evaluated. Pickup noise seen on the baseline level of the PET signals, covered by gradient switching, was eliminated by setting the constant fraction discriminator at a lower energy level of 250 keV. Count rate statistics were similar whether the PET insert was used outside or inside the MR imager. The PET detector ring revealed a point source sensitivity of more than 6% with no MR coil or patient handling device in the FOV of the PET scanner. The energy window for the sensitivity measurement was set between 400 and 650 keV. Cylindrical phantom measurements revealed homogeneity of better than 10% of the reconstructed PET image over a measured interval of 4 hours. For this measurement, all corrections were applied, including calculated attenuation correction since the PET scanner was operated outside the MR system.

Combined MR/PET Imaging and Phantom Studies

The performance of the MR imaging system was not qualitatively influenced by the integrated PET detector ring. Simultaneous MR/PET data acquisition from the Hoffman brain phantom revealed an MR and PET image quality comparable to those of stand-alone systems with no evidence of major artifacts or image distortions (Fig 2a). In a few central sections of the reconstructed PET images, minor ring artifacts were observed owing to the unoptimized state of the PET detector normalization, which was made on the basis of a pseudo-rotating plane source (37 MBq of germanium 68). By using the high-resolution phantom, radioactive rods of 3.0 mm in diameter could be separated at a contrast of 50% (Fig 2b). The Cologne phantom was imaged with high-resolution research tomography (HRRT) (10,15) and shows comparable image resolution, whereas the 2-mm structure can almost be visually identified with HRRT (10). The homogeneity of MR imaging measured with an oil-filled 24-cm homogeneous spheric phantom showed degradations of less than 2 parts per million when measurements were obtained with the PET insert and compared with those obtained without the PET insert. No significant change in background noise was observed and the signal-to-noise ratio remained within the specifications of the MR system.

Combined MR/PET Imaging and Patient Studies

PET and MR image and spectroscopic quality was comparable to that of the corresponding stand-alone scanners (Figs 3, 4). The PET images of FDG uptake showed the typical distribution of cerebral metabolic activity with high values in the cortex, basal ganglia, and thalamus; intermediate values in the cerebellum; and low values in the brainstem and white matter. The spatial resolution was similar to that of HRRT (12) and permitted the identification of small nuclei in the basal brain and in the brainstem (13). The patient who was scanned for restaging of thyroid cancer revealed a normal FDG uptake pattern in the brain. In contrast, the patient with mild cognitive impairment showed some cortical areas and basal ganglia regions with moderately decreased FDG uptake that corresponded to small white matter hyperintensities detected on T2-weighted MR images with increased choline-to-creatine signal intensity ratios on the MR spectroscopic images (Fig 4).

Discussion

The results from phantom and human studies demonstrated that simultaneous high-field-strength MR and PET imaging of the human brain is feasible and the overall performance of each modality is preserved. The integrated LSO-APD

Figure 2

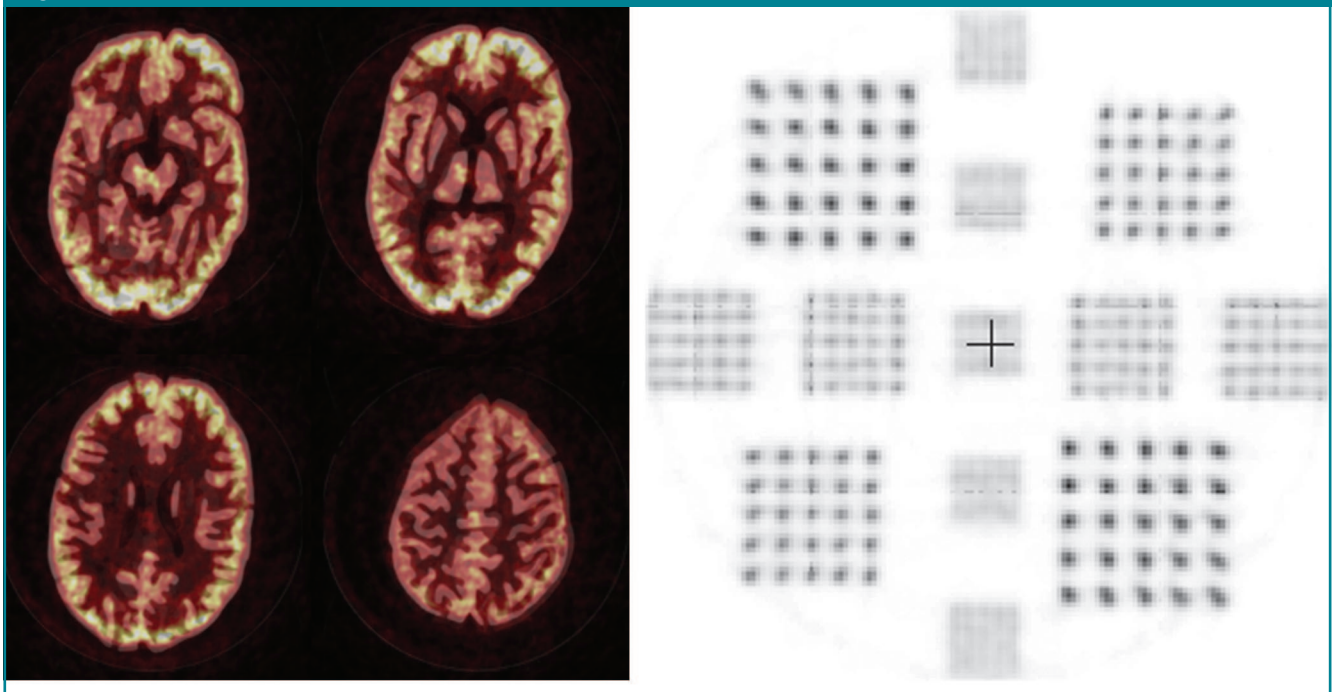

a. b.

Figure 2: **(a)** PET images of Hoffman brain phantom filled with 37 MBq of FDG. Images acquired with MR/PET system demonstrate quality comparable with stand-alone systems with no evidence of artifacts or distortions. **(b)** Cologne phantom—hot rod image shows 3-mm structures (horizontal, central line) that can clearly be separated with 50% contrast. Center spacing between hot rods is twice diameter of hole.

Figure 3

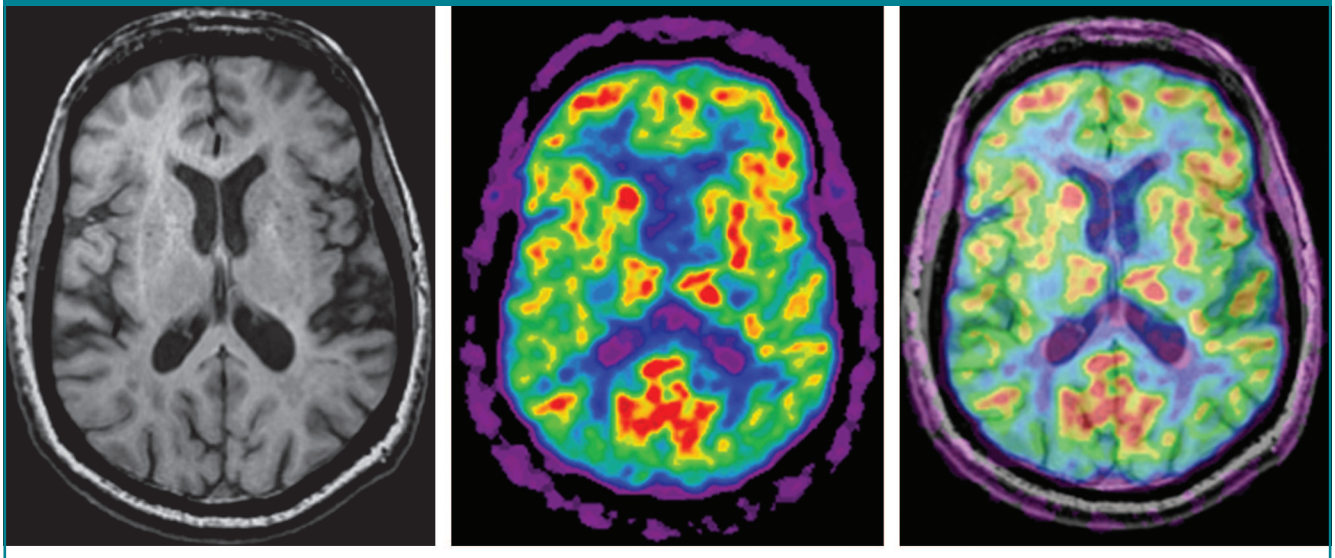

a. b. c.

Figure 3: Simultaneously acquired **(a)** MR, **(b)** PET, and **(c)** superimposed combined MR/PET images of 66-year-old man after intravenous injection of 370 MBq of FDG. Tracer distribution was recorded for 20 minutes at steady state after 120 minutes.

PET detector did not affect the operation of the MR imaging system, and likewise, the PET detector performance was not compromised during MR imaging. The MR/PET data that were simultaneously acquired demonstrated an image quality comparable to stand-alone systems without any major distortions or artifacts. Temporal and spatial intrinsic registration of high-resolution morphologic and functional information in different brain regions enabled accurate matching of FDG uptake and MR signal characteristics. The new MR/PET–inserted PET scanner has a point source sensitivity of more than 6% (PET-only mode). The high sensitivity of the PET scanner and the ability of the combined scanner to acquire multifunction information from PET and MR imaging (eg, functional MR imaging, perfusion- and diffusion-weighted MR imaging, MR spectroscopy) (Fig 4) make the MR/PET system an ideal device for advanced studies of the human brain.

The combined system has several advantages when compared with equivalent freestanding systems: *(a)* The radiation dose is equivalent to stand-alone MR and PET systems because the patient is not exposed to additional ionizing radiation. Moreover, we expect that the PET insert achieves sensitivity that is close to that of brain HRRT (16). Therefore, it can be expected that the overall injected tracer dose might be reduced in the future, minimizing the radiation dose for the patient. *(b)* The scanning time is reduced because of simultaneous data acquisition. *(c)* The qualitative MR image evaluation yielded no obvious image degradation or artifacts compared with conventional brain MR images obtained at 3.0 T. *(d)* No loss of PET image quality was observed when comparing phantom measurements inside and outside the magnet. However, no National Electrical Manufacturers Association measurements were performed at this point. Doyle and ring artifacts that can be seen in the PET images are not related to operation inside the magnet. Rather, they were caused by the unfavorable ratio of the PET system ring diameter and transaxial detector block gaps, required for the geometry of the dedicated brain scanner. Similar effects have been reported for the HRRT brain scanner (17). We are currently working on an improved data normalization procedure. *(e)* All applied MR sequences, including diffusion-weighted imaging and MR spectroscopy, are standard sequences provided by the manufacturer. However, at this stage of engineering, only the transmit/receive head coil has been implemented. Because the PET insert is shielded against electronic pick-up from the radiofrequency coils, further transmit/receive coils that can fit in the PET scanner are, in principle, feasible (eg, a wrist coil).

Figure 4

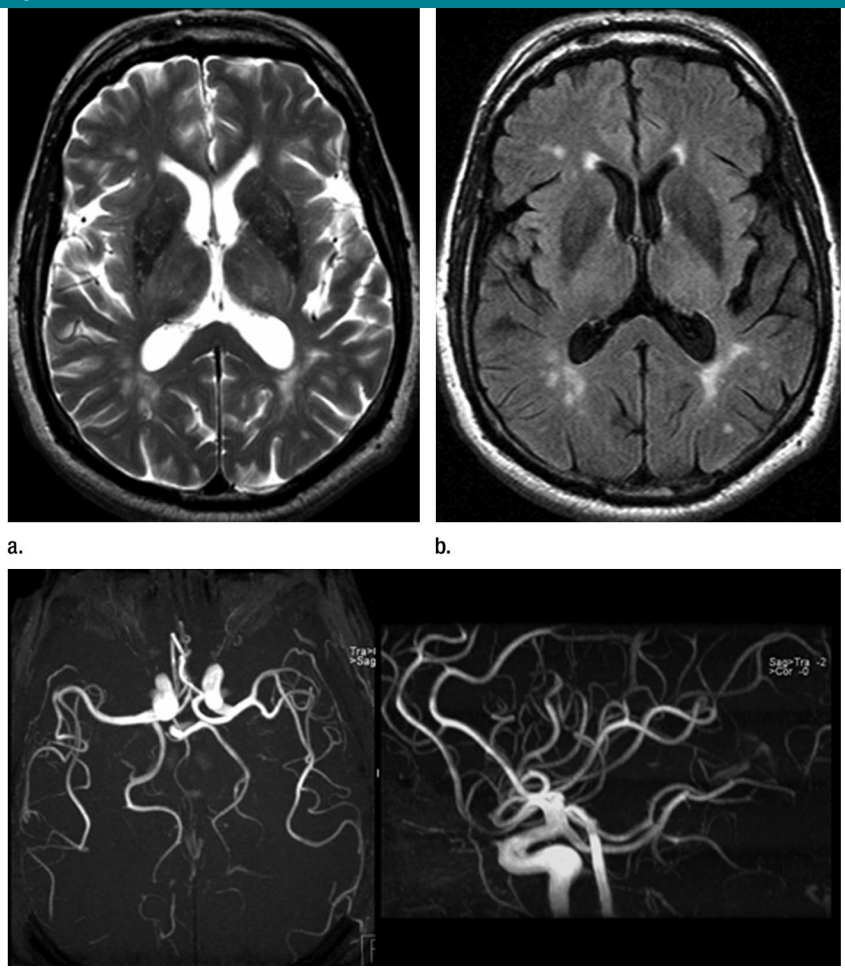

Figure 4: Complete set of acquired MR data of same patient as in Figure 3 includes following imaging sequences: **(a)** T2-weighted turbo spin-echo, **(b)** fluid-attenuated inversion recovery (FLAIR), **(c)** time-of-flight MR angiography. (*Fig 4 continues.*)

Advantages of simultaneous data acquisition include temporal correlation of PET and MR imaging data, reduced imaging time compared with sequential imaging, and improved spatial correlation owing to reduced motion artifacts. Furthermore, cardiac and respiratory motion correction of PET data can be implemented given MR imaging information. Technical challenges of the PET detector system were related to the required MR compatibility, including insensitivity to the high-strength magnetic field and the narrow diameter of the bore of the magnet. The magnetic field– and space-related constraints required a modification of the PET detector tech-

Figure 4 (continued)

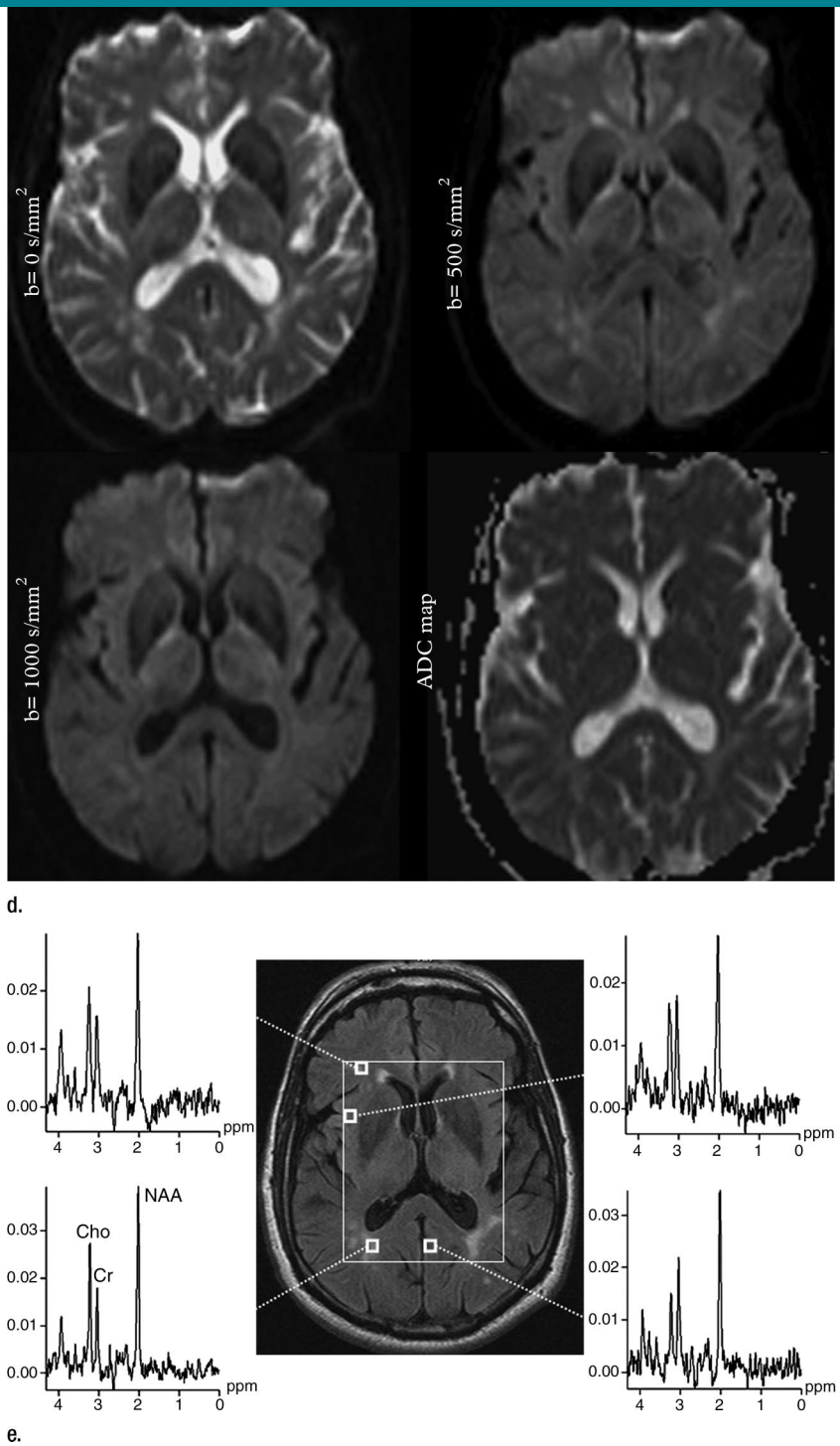

Figure 4 *(continued)*: **(d)** diffusion-weighted MR, and **(e)** proton MR spectroscopic imaging. Increased signal intensities of resonances of choline relative to creatine are apparent in areas of white matter hyperintensities seen on FLAIR images (left spectra) compared with normal gray matter (right spectra). *Cho* = choline, *Cr* = creatine, *NAA* = *N*-acetylaspartate.

nology and geometry, which affected image normalization, the cooling system, and the ability to perform conventional transmission scans for attenuation correction. Accordingly, new methods for MR imaging–based PET attenuation correction have to be developed.

An inherent limitation of PET is that it usually maps only one metabolic, molecular, or functional parameter at a time. Therefore, the metabolic, molecular, or functional objective for PET has to be carefully determined and the tracer must be selected accordingly. However, by using the MR/PET device, several MR-derived morphologic and functional parameters can be observed concurrently with PET imaging. Furthermore, as compared with sequentially acquired MR and PET imaging, the time for data acquisition is notably reduced.

Future applications of MR/PET will include simultaneous acquisition of PET and functional MR imaging combined with diffusion tensor tracking during brain activation studies. In addition, metabolic activity in small cortical areas and in small nuclei of the basal brain and brainstem may be studied by combining the exactly matched functional PET images with the morphologic MR images that are distinguished by using high spatial and contrast resolution. Kinetic studies may include the investigation of dynamic distributions of tracers or drugs in various brain structures and their flow-dependent kinetics, as well as the effects of transmitter/receptor activation on perfusion. Moreover, the development of cell therapy may be monitored (eg, in Parkinson disease). The technique has considerable potential but cannot be fully assessed at this early stage. In any case, the technology will open up a powerful window for brain research and for studies of brain disease.

Limitations of this study included the lack of quantitative data from detailed investigations of mutual interference between the PET and MR imaging from phantom and additional human studies. Further detailed tests that use National Electrical Manufacturers Asso-

ciation measurements and patient examinations are currently planned but are beyond the scope of this initial feasibility report. To bring MR/PET to a stage of accuracy where PET/CT currently is will require considerably more research and technical development.

This proof-of-concept study is focused on brain imaging. Ongoing research in whole-body imaging, particularly with regard to oncology, will afford the opportunity for comprehensive assessment of morphology, perfusion, function, and metabolism in other parts of the body. However, it is unlikely that MR/PET will replace PET/CT. An important advantage of PET/CT is that CT information can be used for PET attenuation correction. The attenuation correction for PET on the basis of MR imaging information is still challenging, although some early approaches have produced promising results (18). Nevertheless, substantial scientific and clinical progress can be anticipated by using and advancing this MR/PET technology.

In conclusion, simultaneous high-field-strength MR and PET imaging of the human brain is feasible and the overall performance of each modality is preserved.

References

1. Beyer T, Townsend DW, Brun T, et al. A combined PET/CT scanner for clinical oncology. J Nucl Med 2000;41(8):1369–1379.
2. Goerres GW, von Schulthess GK, Steinert HC. Why most PET of lung and head-and-neck cancer will be PET/CT. J Nucl Med 2004;45(suppl 1):66S–71S.
3. Muller-Horvat C, Radny P, Eigentler TK, et al. Prospective comparison of the impact on treatment decisions of whole-body magnetic resonance imaging and computed tomography in patients with metastatic malignant melanoma. Eur J Cancer 2006;42(3):342–350.
4. Pfannenberg C, Aschoff P, Schanz S, et al. Prospective comparison of 18F-fluorodeoxyglucose positron emission tomography/computed tomography and whole-body magnetic resonance imaging in staging of advanced malignant melanoma. Eur J Cancer 2007;43(3):557–564.
5. Pichler BJ, Judenhofer MS, Catana C, et al. Performance test of an LSO-APD detector in a 7-T MRI scanner for simultaneous PET/MRI. J Nucl Med 2006;47(4):639–647.
6. Melcher CL, Schweitzer JS. Cerium-doped lutetium oxyorthosilicate: a fast, efficient new scintillator. IEEE Trans Nucl Sci 1992;39(4):502–505.
7. Pichler B, Lorenz E, Mirzoyan R, et al. Performance test of a LSO-APD PET module in a 9.4 Tesla magnet. In: Conference Record of the 1998 Institute of Electrical and Electronics Engineers (IEEE) Nuclear Science Symposium and Medical Imaging Conference. Piscataway, NJ: IEEE, 1998;1237:–1239.
8. Judenhofer MS, Catana C, Swann BK, et al. PET/MR images acquired with a compact MR-compatible PET detector in a 7-T magnet. Radiology 2007;244(3):807–814.
9. Hoffman EJ, Cutler PD, Digby WM, et al. 3-D phantom to simulate cerebral blood flow and metabolic images for PET. IEEE Trans Nucl Sci 1990;37(2):616–620.
10. Schmand M, Wienhard K, Casey ME, et al. Performance evaluation of a new LSO high resolution researchtomograph-HRRT. In: Conference Record of the 1999 Institute of Electrical and Electronics Engineers (IEEE) Nuclear Science Symposium and Medical Imaging Conference. Piscataway, NJ: IEEE, 1999;1067:–1071.
11. Comtat C, Bataille F, Michel C, et al. OSEM-3D reconstruction strategies for the ECAT HRRT. In: Conference Record of the 2004 Institute of Electrical and Electronics Engineers (IEEE) Nuclear Science Symposium and Medical Imaging Conference. Piscataway, NJ: IEEE, 2004;3492:–3496.
12. Byars LG, Sibomana M, Burbar Z. Variance reduction on randoms from delayed coincidence histograms for the HRRT. In: Conference Record of the 2005 Institute of Electrical and Electronics Engineers (IEEE) Nuclear Science Symposium and Medical Imaging Conference. Piscataway, NJ: IEEE, 2005;2622:–2626.
13. Watson CC, Casey ME, Michel C, Bendriem B. Advances in scatter correction for 3D PET/CT. In: Conference Record of the 2004 Institute of Electrical and Electronics Engineers (IEEE) Nuclear Science Symposium and Medical Imaging Conference. Piscataway, NJ: IEEE, 2004;3008:–3012.
14. Vollmar S, Hampl JA, Kracht L, et al. Integration of functional data (PET) into brain surgery planning and neuronavigation. In: Buzug TM, ed. Advances in medical engineering: proceedings in physics 114. Berlin, Germany: Springer, 2007;98:–103.
15. Wienhard K, Schmand M, Casey ME, et al. The ECAT HRRT: performance and first clinical application of the new high resolution research tomograph. IEEE Trans Nucl Sci 2002;49(1):104–110.
16. Heiss WD, Habedank B, Klein JC, et al. Metabolic rates in small brain nuclei determined by high-resolution PET. J Nucl Med 2004;45(11):1811–1815.
17. Vollmar S, Michel C, Treffert JT, et al. HeinzelCluster: accelerated reconstruction for FORE and OSEM3D. Phys Med Biol 2002;47(15):2651–2658.
18. Hofmann M, Steinke F, Scheel V, et al. MR-based attenuation correction for PET/MR: a novel approach combining pattern recognition and atlas registration. J Nucl Med 2008 [in press].